Respiratory Physiology & Neurobiology 333 (2025) 104397

Contents lists available at ScienceDirect

Respiratory Physiology & Neurobiology

journal homepage: www.elsevier.com/locate/resphysiol

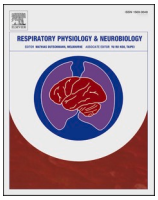

A computational fluid dynamics analysis of BiPAP pressure settings on airway biomechanics using a CT-based respiratory tract model

Xinlei Huang [a], Goutam Saha [a], Akshoy Ranjan Paul [b], Adele Tahan [c], Suvash C. Saha [a,*]

[a] School of Mechanical and Mechatronic Engineering, Faculty of Engineering and Information Technology, University of Technology Sydney, Sydney, NSW 2007, Australia
[b] Motilal Nehru National Institute of Technology Allahabad, Prayagraj 211004, India
[c] Adore Pharmacy, Community Pharmacy, 671 Darling St, Rozelle, NSW 2039, Australia

ARTICLE INFO

Edited by M. Dutschmann

Keywords:
Bilevel positive air pressure
Human respiratory tract
Sleep apnea
Chronic obstructive pulmonary disease
Obesity hypoventilation syndrome
Health

ABSTRACT

Central and Obstructive Sleep Apnea (CSA and OSA), Chronic Obstructive Pulmonary Disease (COPD), and Obesity Hypoventilation Syndrome (OHS) disrupt breathing patterns, posing significant health risks and reducing the quality of life. Bilevel Positive Airway Pressure (BiPAP) therapy offers adjustable inhalation and exhalation pressures, potentially enhancing treatment adaptability for the above diseases. This is the first-ever study that employs Computational Fluid Dynamics (CFD) to examine the biomechanical impacts of BiPAP under four settings: Inspiratory Positive Airway Pressure (IPAP)/Expiratory Positive Airway Pressure (EPAP) of 12/8, 16/6, and 18/8 cmH_2O, compared to a without-BiPAP scenario of zero-gauge pressure. Utilizing a computed-tomography-based respiratory tract model from the nasal cavity extending to the 13th generation, we analyzed parameters such as static pressure, shear stress, and airway wall normal force across different airway regions. Our results indicate that BiPAP, particularly at higher IPAP settings, effectively increases static pressure, thereby improving airway patency and potentially reducing the risk of airway collapse in both CSA and OSA. Lower EPAP, on the other hand, helps reduce the work of breathing during exhalation, which is particularly useful for patients who have difficulty exhaling against higher pressures or need to exhale CO_2 more effectively. This comparative analysis confirms that BiPAP not only maintains open airways but does so with an adjustable approach that can be used for the specific needs of patients with various respiratory dysfunctions, thereby offering a versatile and effective treatment option.

1. Introduction

Sleep-related breathing disorders, including Central Sleep Apnea (CSA), Obstructive Sleep Apnea (OSA), Obesity Hypoventilation Syndrome (OHS), and Chronic Obstructive Pulmonary Disease (COPD), represent a significant health burden with complex interrelationships and multifaceted impacts on patient health. Central sleep apnea occurs when the brain fails to send the proper signals to the muscles controlling breathing during sleep, leading to periodic breathing interruptions (Javaheri and Badr, 2022; Sanchez et al., 2020; Tung et al., 2017; Tung and Anter, 2016). Obstructive sleep apnea involves the partial or complete blockage of the upper airway during sleep, interrupting normal breathing (McNicholas, 2009; Donovan and Kapur, 2016; Dunlap et al., 2023). It is also recorded the occurrence of mixed sleep apnea, a combination of CSA and OSA (Yang et al., 2019). Obesity hypoventilation syndrome is characterized by obesity coupled with chronic hypoventilation, leading to complications such as pulmonary hypertension (Olson and Zwillich, 2005; Young and Benjamin, 2023; Agossou et al., 2023). Moreover, obesity may also cause upper airway obstruction, which ultimately leads to the development of OSA (Al-Abri and BaHammam, 2023). Chronic obstructive pulmonary disease is a progressive and non-reversible lung disease characterized by the gradual development of dyspnea, sputum production, and severe cough due to chronic inflammation (Agrawal et al., 2019; Singh et al., 2019; Petty, 2006; Raherison and Girodet, 2009). Collectively, these disorders severely impact patient health, contributing to cardiovascular diseases, daytime fatigue, systemic inflammation, and increased mortality risk. The intermittent hypoxia and sleep fragmentation associated with CSA, OSA, and OHS may eventually lead to significant cardiovascular burden and neurocognitive dysfunction, while COPD's progressive nature exacerbates respiratory insufficiency, reducing quality of life and

* Corresponding author.
E-mail address: Suvash.Saha@uts.edu.au (S.C. Saha).

https://doi.org/10.1016/j.resp.2025.104397
Received 13 November 2024; Received in revised form 6 January 2025; Accepted 13 January 2025
Available online 16 January 2025

Nomenclature

Roman symbols

F_2	blending function for Eq. (6)
g	gravitational acceleration, which queals to 9.81 (ms^{-2})
k	turbulence kinetic energy (m^2s^{-2})
p	static pressure (Pa)
t	time (s)
u	fluid velocity vector (ms^{-1})
G_b	turbulence generation due to buoyancy
$G_{\omega b}$	turbulence generation due to buoyancy for ω equation
P_k	rate of production of turbulent kinetic energy
Pr_t	turbulent Prandtl number
P_ω	rate of production of specific dissipation rate
S	strain rate magnitude (s^{-1})
S_{ij}	mean component of the rate of deformation s_{ij}
x_i, x_j	a unit of Cartesian coordinate
y	distance to the next surface
Y_k	dissipation of turbulent kinetic energy due to turbulence
Y_ω	dissipation of specific dissipation rate due to turbulence

Greek symbols

α	model constant, which is equal to 0.44
α^*	damping coefficient
σ_k	turbulent Prandtl number for turbulent kinetic energy
σ_ω	turbulent Prandtl number for the specific dissipation rate
μ	molecular viscosity (Nsm^{-2})
μ_t	turbulent viscosity (Nsm^{-2})
ν	kinematic viscosity of the air (m^2s^{-1})
ρ	air density(kgm^{-3})
$\bar{\tau}$	stress tensor (Pa)
ω	specific dissipation rate (s^{-1})

longevity.

Given the significant respiratory challenges posed by CSA, OSA, OHS and COPD, the therapeutic use of Positive Airway Pressure (PAP) devices offers a critical intervention to manage and improve patient outcomes in these conditions (Agossou et al., 2023; Pazarli and Köseoğlu, 2023). Specifically, the BiPAP therapy, a non-invasive ventilation approach, provides two distinct pressure levels that are particularly beneficial in supporting patients with these complex respiratory conditions. Inspiratory Positive Airway Pressure (IPAP) controls the peak pressure during inhalation, providing the necessary force to augment the patient's inspiratory effort and improve ventilation, while Expiratory Positive Airway Pressure (EPAP) controls the pressure during exhalation, maintaining airway patency and preventing airway collapse (Gay et al., 2003). By alternating between these two pressure levels, BiPAP therapy effectively enhances respiratory mechanics, improves gas exchange (Pazarli and Köseoğlu, 2023), and relieves the symptoms associated with various respiratory disorders.

Over the past two decades, the application of Computational Fluid Dynamics (CFD) has expanded significantly (Huang et al., 2022), revolutionizing our understanding of physiological phenomena in both healthy and pathological states (Saha et al., 2024a). Recent research has validated CFD as a robust tool for diagnosing (Ryu et al., 2021) and evaluating (Taherian et al., 2019) OSA, assessing the impact of adenoidal and tonsillar hypertrophy on the severity of pediatric OSA (Iwasaki et al., 2020), and analyzing airflow dynamics within the upper airway of OSA patients, both under the open oral cavity conditions (Chen et al., 2021) and post-operative scenarios (Nomura et al., 2022). In the context of COPD research, CFD has been employed not only for diagnosing obstructions (Hu et al., 2022) but also for a detailed analysis that is challenging to achieve via *in-vivo* methods, such as small airway resistance (Zhang et al., 2024) and mucus clearance effectiveness (Ren et al., 2020). Advances have been made by integrating CFD with fluid-structure interaction (FSI) models to simulate the dynamics of emphysematous alveolar sacs (Carotenuto et al., 2023), and combining CFD with the particle dynamics to investigate particle transport and deposition within the COPD-affected airways (Kadota et al., 2022).

However, a significant gap persists in the literature, as no CFD study has yet explored the effects of BiPAP on respiratory mechanics. The current literature lacks comprehensive data on air pressure, shear stress, and forces on the airway walls during BiPAP treatment. The present study aims to address this gap by conducting pioneering CFD simulations based on realistic computed tomography (CT) scans of the entire respiratory tract, thereby examining the biomechanical impacts of BiPAP under various conditions: IPAP/EPAP settings of 12/8 cmH_2O typically recommended for CSA and OSA (American Academy of Sleep Medicine et al., 2008; Blau et al., 2012); 16/6 cmH_2O for COPD (Bhatt et al., 2013; Paone et al., 2014; Funk et al., 2011); and 18/8 cmH_2O for OHS (Borel et al., 2012; Masa et al., 2015, 2016), as compared to a baseline scenario of zero gauge pressure. To remove patient-specific factors and focus on broader flow phenomena, the BiPAP settings were chosen based on values recommended by previous research rather than any individual patient prescription. By simulating the biomechanical impacts of BiPAP across various prescribed settings, the present research could lead to optimized pressure settings customized to the specific needs of different patient groups, thus improving therapeutic outcomes. Moreover, the detailed biomechanical insights gained could inform the design of more effective BiPAP machines and interfaces, ultimately contributing to better patient compliance and comfort. This study represents a critical step toward the personalized medicine approach in the management of respiratory disorders.

2. Methodology

2.1. Computational model of the respiratory tract

This study focuses on the development of a comprehensive computational model for the human respiratory tract, incorporating detailed methodologies and advanced meshing techniques to ensure high precision and accuracy. The segmentation of highly detailed three-dimensional surface models from the CT images was performed using Mimics Medical 21 (Medical, 2021), followed by surface sectioning and enhancement with the Geomagic Wrap 2021 (GeomagicWrap, 2022), and post-processing was carried out in Siemens NX 12 (Siemens, 2017) to refine the model. This refined model was then transferred to Ansys (ANSYS, 2020a) for meshing and simulation, resulting in a sophisticated representation of the respiratory tract, as detailed in our prior works (Saha et al., 2022a,b). The final model, as shown in Fig. 1(a), includes significant anatomical details and was optimized for meshing and simulation by simplifying the anatomical components into distinct regions: nasal cavity, nasopharynx, oral cavity, oropharynx, larynx, laryngopharynx, and airways from generation (G) 0–13. The development of this model using human CT scans received necessary ethical approval from the Human Research Ethics Committees at the University of Technology Sydney vide ethical approval reference ETH23–8670 dated 7 September 2023.

2.2. Governing equations

This study employs the continuity and momentum equations to model the aerodynamics of the respiratory tract. The *k–ω* Shear Stress

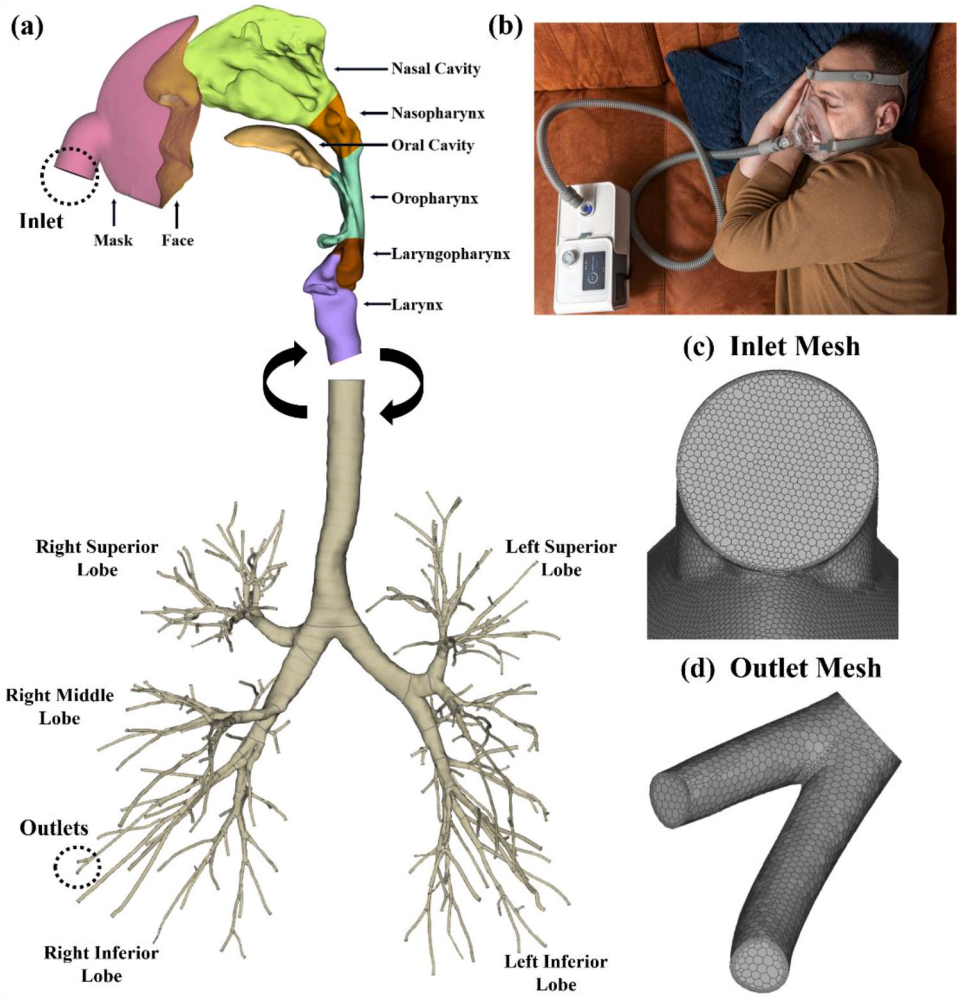

Fig. 1. Visual representations showing: (a) present study's computational model of the human respiratory tract; (b) use of BiPAP machine by a patient; the polyhedral discretization scheme and the thickness-changing boundary layer at the (c) mask inlet and (d) bronchioles' outlets.

Transport (SST) turbulence model (ANSYS, 2020b) was utilized to capture inherent turbulence phenomena. This model adeptly integrates the strengths of both k–ε and k–ω models, enhancing the precision of predictions related to adverse pressure gradients—an essential aspect of the respiratory tract geometry. The governing equations applied are listed as follows:

Continuity equation:

$$\frac{\partial \rho}{\partial t} + \nabla \bullet (\rho \boldsymbol{u}) = 0 \tag{1}$$

Momentum equation:

$$\frac{\partial \rho \boldsymbol{u}}{\partial t} + \nabla \bullet (\rho \boldsymbol{u}\boldsymbol{u}) = -\nabla p + \nabla \bullet (\bar{\tau}) + \rho \boldsymbol{g} \tag{2}$$

Turbulent kinetic energy equation:

$$\frac{\partial (\rho k)}{\partial t} + \frac{\partial (\rho k u_i)}{\partial x_i} = \frac{\partial}{\partial x_j}\left[\left(\mu + \frac{\mu_t}{\sigma_k}\right)\frac{\partial k}{\partial x_j}\right] + P_k - Y_k + G_b \tag{3}$$

Specific dissipation rate equation:

$$\frac{\partial (\rho \omega)}{\partial t} + \frac{\partial (\rho \omega u_i)}{\partial x_i} = \frac{\partial}{\partial x_j}\left[\left(\mu + \frac{\mu_t}{\sigma_\omega}\right)\frac{\partial \omega}{\partial x_j}\right] + P_\omega - Y_\omega + G_{\omega b} \tag{4}$$

In SST turbulence model, the eddy-viscosity in Eqs. (3) and (4) are formulated as:

$$\mu_t = \frac{\rho k}{\omega}\frac{1}{\max\left[\frac{1}{\alpha^*}, \frac{SF_2}{0.31\omega}\right]} \tag{5}$$

Where the damping coefficient $\alpha^*$is given by:

$$\alpha^* = \left(\frac{0.024 + \frac{\rho k}{6\mu\omega}}{1 + \frac{\rho k}{6\mu\omega}}\right) \tag{6}$$

And the blending function F_2 is defined as:

$$F_2 = \tanh\left\{\left(\max\left[2\frac{\sqrt{k}}{0.09\omega y}, \frac{500\mu}{\rho y^2 \omega}\right]\right)^2\right\} \tag{7}$$

The turbulence generation due to buoyancy term G_b in Eq. (3) is given by:

$$G_b = -g_i \frac{\mu_t}{\rho \mathrm{Pr}_t}\frac{\partial \rho}{\partial x_i} \tag{8}$$

The buoyancy source term $G_{\omega b}$ in Eq. (4) is defined as:

$$G_{\omega b} = \frac{\omega}{k}\left[(1+\alpha)\tanh\left|\frac{\nu}{u}\right| G_b - G_b\right] \tag{9}$$

where all the units and values of the symbols and constant terms are

explained in the Nomenclature. The continuity equation (Eq. (1)) ensures mass conservation, maintaining the equilibrium of air entering and exiting a region within the respiratory tract, crucial for understanding respiratory mechanics. The momentum equation (Eq. (2)), derived from Newton's second law, provides a framework for analyzing how forces and pressure gradients influence airflow, detailing the interactions between mass flow, pressure, and acceleration. The turbulent kinetic energy (TKE) equation (Eq. (3)) quantifies the energy associated with chaotic air particle motion in turbulent flow, serving as a measure of turbulence intensity. The specific dissipation rate equation (Eq. (4)) calculates the rate at which TKE dissipates within the flow, offering insights into energy transformations during turbulence. Eqs. (5)–(9) are the modeling components of the SST turbulence model that explain the eddy viscosity, damping coefficient, blending function, and source term due to buoyancy for the TKE and specific dissipation transport equations, respectively.

2.3. Numerical framework

This study models the complex geometry of the respiratory tract for transient simulation using advanced computational techniques. A polyhedral hybrid mesh with hexagonal prisms in the boundary layers and irregular polyhedral cells in the volume, totaling approximately 7.75 million cells, was employed to capture near-wall fluid dynamics. The mesh design features a changing nodal distance, decreasing from 0.4 mm in the upper airway to 0.2 mm in the smaller bronchial branches, as shown in Fig. 1(c) and (d).

The velocity boundary profiles were derived from experimentally determined flow distributions, ensuring realistic velocity magnitude and direction at the boundaries. The velocity at each lobe's outlet was calculated using the formula: Lobe velocity = (Total volume flow rate × Lobe flow percentage) / Lobe outlet area. The total volume flow rate in the formula was experimentally measured (Nishi, 2004) and adopted in CFD for slow breathing conditions (15 breaths per minute) (Wedel et al., 2022), as shown in Fig. 2. (a). This study aims to examine the biomechanical impacts of BiPAP therapy under three different settings: IPAP and EPAP of 12/8, 16/6, and 18/8 cmH_2O, which is typically recommended for CSA and OSA, COPD, and OHS, respectively. The three BiPAP pressure profiles, as well as a zero-gauge ambient pressure profile, are shown in Fig. 2(b).

2.4. Validation and verification of CFD model

The numerical methodology employed in this study was extensively validated and verified in our previous studies, demonstrating robust performance across several key metrics. Specifically, we have rigorously evaluated the accuracy of the pressure field (Saha et al., 2022a) through comparisons with the previous numerical studies, assessing the dynamics of mass transfer rates and velocity fields (Saha et al., 2024b; Huang et al., 2024b) against the established benchmarks from numerical and experimental data, and finally validated various thermodynamic properties (Huang et al., 2024a; Saha et al., 2022a) through comparisons with both higher-order calculation schemes and prior numerical and experimental studies. Furthermore, comprehensive mesh independence tests were conducted (Huang et al., 2024a,b; Saha et al., 2024b), indicating that our respiratory tract model can achieve mesh independence with 7.75 million polyhedral cells and four layers of dynamically changing boundary layer mesh (Fig. 1(b) and (c)) under both k–ω and large eddy simulation (LES) turbulence models.

2.5. Limitation of the model

This study does not incorporate thermal boundary conditions, nor does it model the two layers of airway wall liquids—serum and mucus—and their evaporation processes. Despite these omissions, the simplifications adopted significantly reduced computational complexity without substantially affecting the airflow dynamics, which are the primary focus of this research. This approach aligns with modeling methodologies employed in prior and recent studies (Wedel et al., 2022; Gökcan et al., 2024; Gunatilaka et al., 2020).

3. Results and discussion

The numerical results are post-processed, visualized and discussed in this section. The following subsections provide a detailed analysis of the velocity field, static pressure field, wall shear stress, and area- and time-averaged statistics, including average wall pressure and wall-normal force during inhalation and exhalation.

3.1. Velocity dynamics in the upper airways

The Z-velocity contour of Fig. 3 depicts airflow velocities within the upper respiratory tract under a BiPAP setting of 12/8 cmH_2O. The range of airflow velocities is indicated by the color gradient from red to blue,

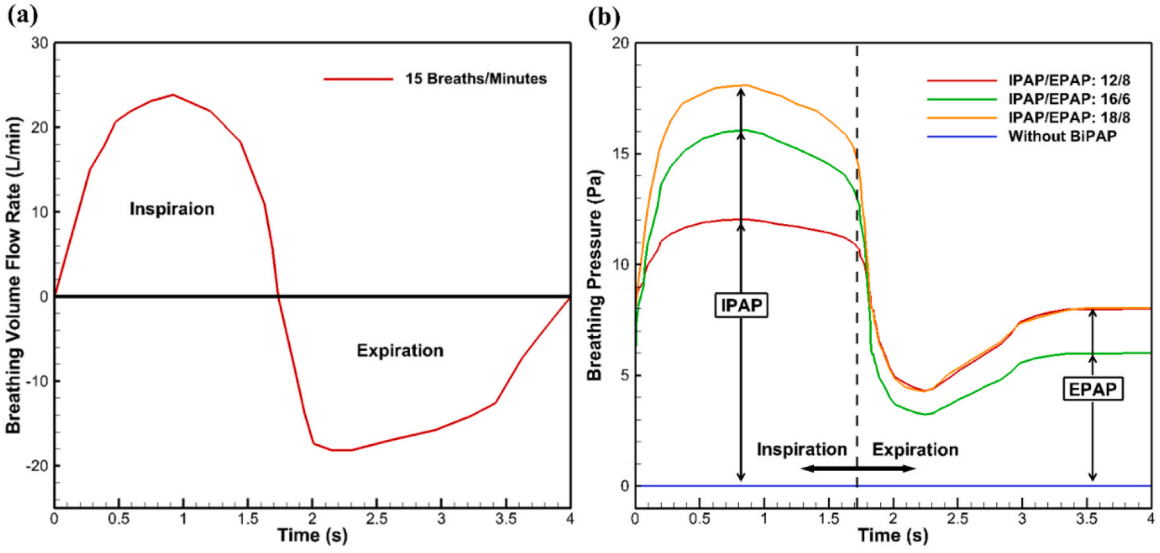

Fig. 2. Realistic boundary conditions showing (a) volume flow rate during one respiration, and (b) pressure profiles applied at the mask inlet.

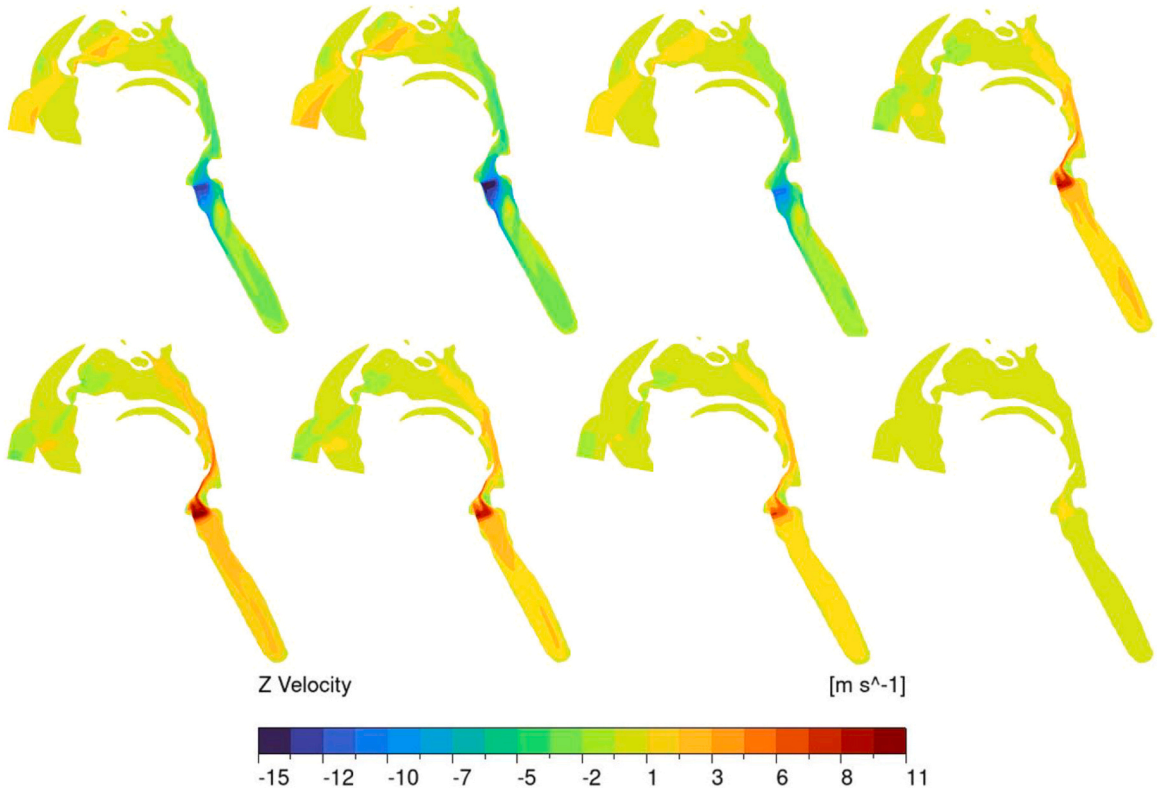

Fig. 3. Z-velocity contour of the upper airway under IPAP/EPAP 12/8 cmH_2O. The contours are similar in all four cases.

representing inhalation (positive velocity) to exhalation (negative velocity). The high-velocity zones, notably in the nasal cavity entrance, suggest robust airflow during inhalation. The lower parts of the airway show decreased velocities, depicted in blue and green, indicating a slowdown during exhalation or due to the natural narrowing of the airway.

When comparing the velocity contour of different pressure boundary setting, it seems the pressure adjustments have minimal impact on these velocity profiles. The consistency of the airflow pattern across different settings implies that the physical structure of the airway and the inherent airflow mechanics play more significant roles in determining the velocity field than the pressure settings themselves.

3.2. *Pressure dynamics in upper and lower airways*

The graphs in Fig. 4 represent the area-weighted average wall static pressure in various sections of the respiratory tract under different BiPAP settings, including the without-BiPAP scenario. The baseline scenario without BiPAP shown in Fig. 4(a) and (b) indicates relatively low and uniform static pressures across different airway regions, suggesting minimal airway support and potential for collapse, particularly in patients prone to sleep apnea.

As the BiPAP settings are introduced, with IPAP/EPAP settings of 12/8, 16/6, and 18/8 cmH_2O, a progressive increase in static pressures is observed. The setting of 12/8 cmH_2O in Fig. 4(c) and (d) shows a moderate pressure enhancement, sufficient to maintain airway patency but not as pronounced as in higher settings. This suggests its potential applicability for patients requiring minimal intervention. Moving to the 16/6 cmH_2O setting shown in Fig. 4(e) and (f), there is a notable increase in static pressure, particularly in the nasal cavity and nasopharynx. This setting offers robust support against airway collapse during inhalation while allowing easier exhalation due to reduced expiratory pressure, benefitting CO_2 removal and reducing the work of breathing in patients with COPD.

The highest pressures are experienced with the 18/8 cmH_2O setting shown in Fig. 4(g) and (h), indicating the strongest support against airway collapse. This configuration ensures that the airways remain open during inhalation and exhalation, making it suitable for patients with severe OHS, where maintaining airway patency is critical. However, the application of higher pressure must be balanced against potential risks such as discomfort or the development of air leaks, which could diminish patient compliance with the therapy.

In the without-BiPAP scenario (Fig. 4a and b), the static pressure profile across the airway regions from the nasal cavity to the larynx typically exhibits a pattern of a gradual decline followed by a subsequent rise. This pattern is driven by the mechanics of inhalation, during which the diaphragm contracts and descends, and the ribcage expands, creating a negative pressure lower than atmospheric levels within the airway. The inverse phenomena occur during exhalation, where positive pressure is generated as the diaphragm relaxes and the ribcage contracts, aiding in expelling air from the lungs. Conversely, the pressure profiles under BiPAP settings distinctly display an initial rise in the static pressure, particularly in the nasal and nasopharyngeal regions, which is subsequently reduced toward the larynx. This elevation at the beginning of the airways is attributed to the externally applied positive pressure by the BiPAP system, designed to open and stabilize the airways forcibly. Both inspiratory and expiratory pressures provided by the BiPAP machine are increased, effectively raising the airway's static pressure and offsetting the natural pressure drop observed during the without-BiPAP scenarios.

The static pressure contours depicted across different BiPAP settings in Fig. 5 provide a detailed understanding of the distribution and impact of positive airway pressures within the upper respiratory tract under varying therapeutic conditions. The Fig. 5 (I) corresponds to an IPAP/EPAP ratio of 12/8 cmH_2O and shows a moderate positive pressure environment. This uniform distribution from the nasal cavity to the larynx underlines a balanced application of pressure that adequately supports the airway patency without exerting excessive force, making it

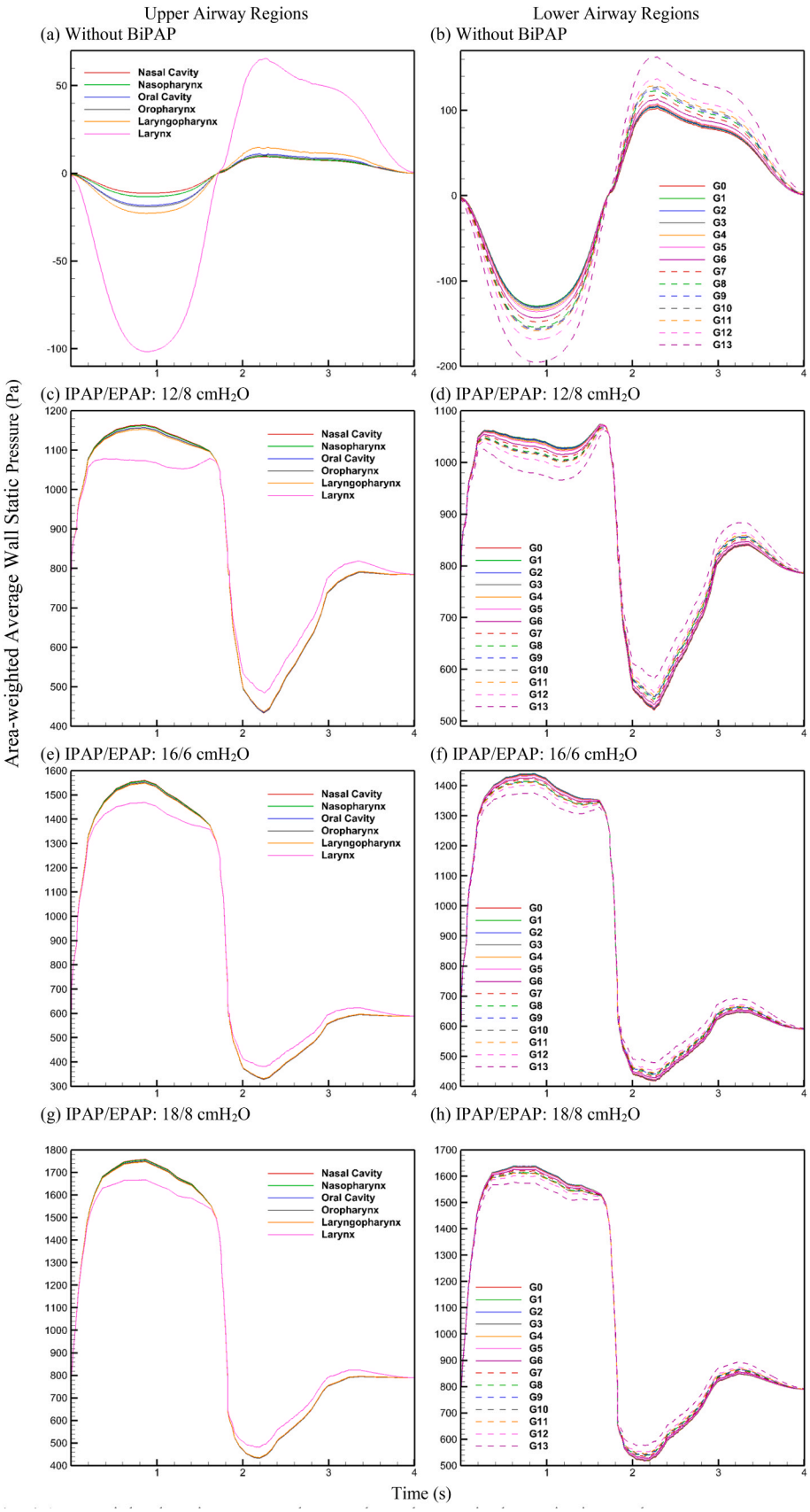

Fig. 4. Area-weighted static pressure changes throughout a single respiration cycle.

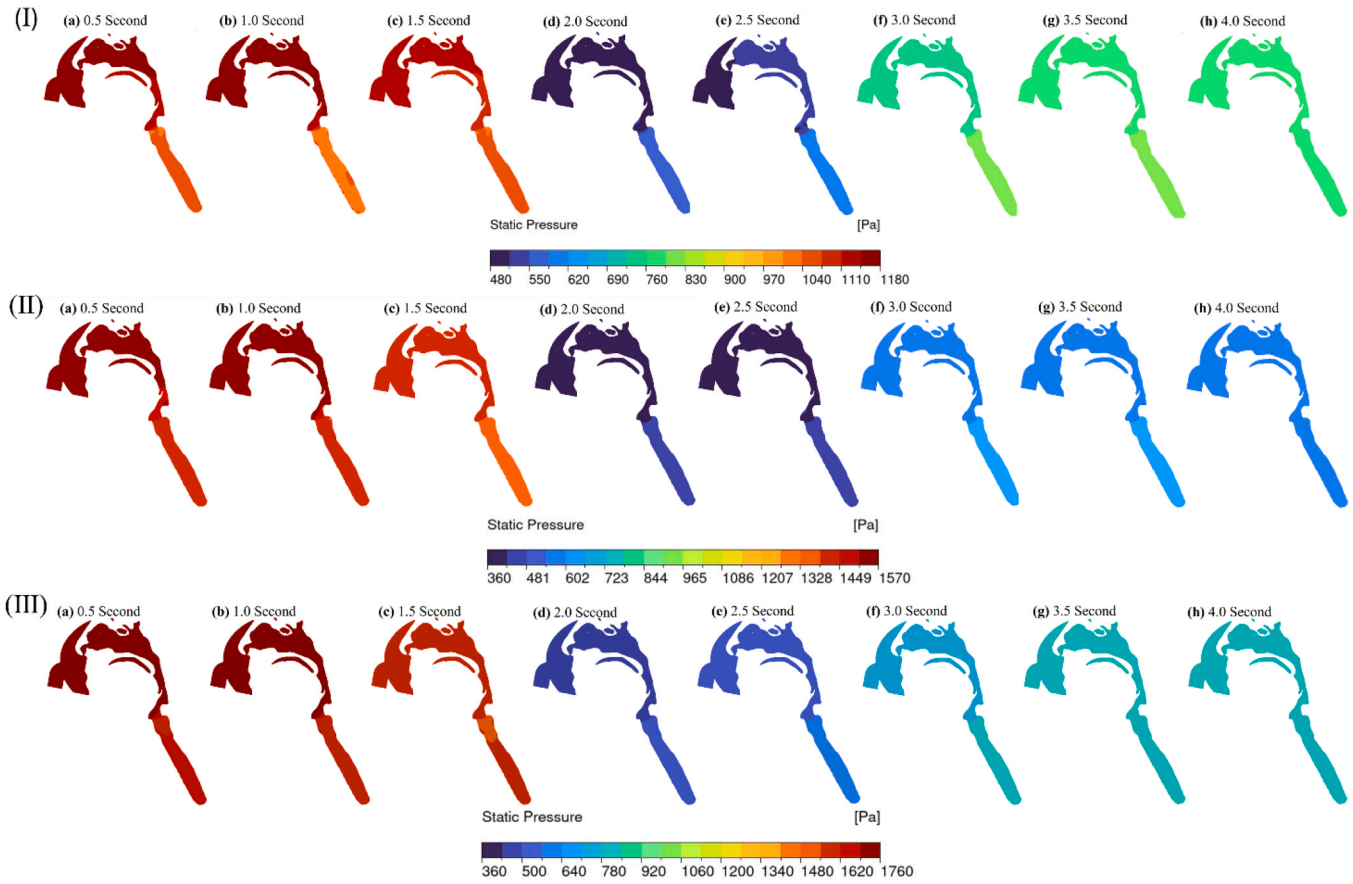

Fig. 5. Static pressure contour of the upper airway under IPAP/EPAP of (I) 12/8 cmH_2O, (II) 16/6 cmH_2O, and (III) 18/8 cmH_2O condition.

suitable for patients who require a moderate level of support to prevent airway collapse.

Moving to a more intensified setting of 16/6 cmH_2O, as illustrated in Fig. 5 (II), there is a noticeable escalation in pressure, primarily concentrated in the nasal cavity and nasopharynx. This increment aligns with the higher IPAP of 16 cmH_2O, designed to forcefully stabilize the airway, which could be critical for patients experiencing significant airway obstructions during sleep. The reduction in EPAP to 6 cmH_2O is clearly visualized by the diminished pressure during the exhalation phase, which is crucial for reducing the exhalatory resistance, thereby aiding patients who struggle with higher pressures during exhalation.

Fig. 5 (III) represents the highest IPAP/EPAP setting of 18/8 cmH_2O and showcases an extensive application of positive pressures throughout the airway. The broad and intense pressure distribution supports a substantial mechanical opening and stabilization of the airway, indicated by the high IPAP of 18 cmH_2O. The corresponding EPAP of 8 cmH_2O, while providing sufficient reduction to aid exhalation, does not diminish as much as the previous lower setting, indicating a therapy suited for patients requiring significant assistance during inhalation but capable of managing a slightly elevated pressure during exhalation.

These visual insights into the pressure dynamics across different therapeutic settings highlight the critical role of customizing BiPAP pressures to the specific needs of patients. The ability to adjust IPAP and EPAP ensures that the therapy not only supports airway patency but also optimizes patient comfort and compliance, particularly in managing diverse conditions of sleep-related breathing disorders. The strategic application of varying pressure provides a compelling approach to enhancing the efficacy and adaptability of BiPAP therapy in clinical practice.

3.3. Airway shear stress

Fig. 6 presents a visualization of area-weighted shear stress changes throughout a single respiration cycle. This analysis is essential in understanding the biomechanical forces at play during natural breathing and under therapeutic interventions like mechanical ventilation.

In the upper airway region, Fig. 6(a) reveals differences in shear stress across various anatomical structures. The larynx and laryngopharynx exhibit noticeable peaks in shear stress around the midpoint of the inhalation and exhalation phases, corresponding to the peak in volume flow rate of air shown in Fig. 6(a). This suggests that the higher-velocity airflow entering and exiting through these narrow passages imposes mechanical stress on the airway walls. In contrast, the nasal cavity and nasopharynx demonstrate lower stress levels, a phenomenon that can be attributed to their broader cross-sectional areas, which dissipate airflow velocity and reduce the resultant mechanical stress.

Transitioning to the lower respiratory tract shown in Fig. 6(b), the shear stresses observed are generally lower than in the upper airways, reflecting the branching nature of the bronchial tree, which increases total cross-sectional area and reduces stress per unit area. The coherent pattern of stress across these generations, peaking uniformly around the peak inhalation and exhalation phase, illustrates a uniform transmission of respiratory effort through the lower airways. The increase of stress from proximal to distal generations indicates an increase in mechanical load further from the trachea.

High shear stresses in the upper airways have been identified as potential risks for mucosal damage or irritation, leading to the growth of lesions in many occurrences. However, recent data suggests that using BiPAP does not significantly alter the airway wall shear stress level. This observation indicates that BiPAP therapy supports respiratory function

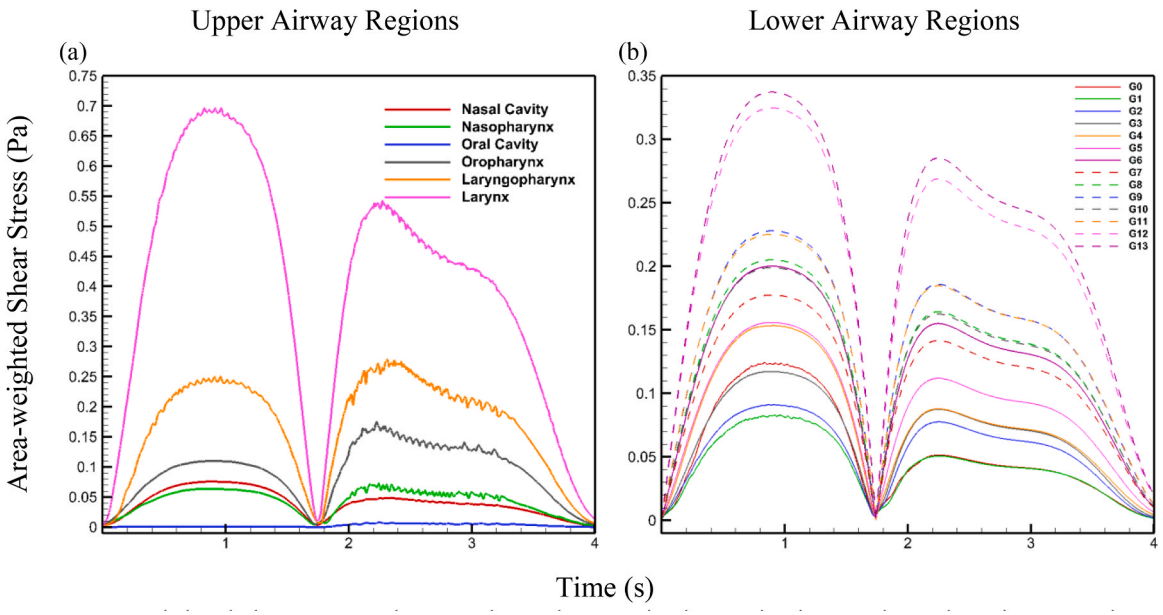

Fig. 6. Area-weighted shear stress changes throughout a single respiration cycle under BiPAP settings.

effectively without exacerbating mechanical stress on the airway walls. This finding is particularly significant in the context of respiratory therapy, suggesting that BiPAP can offer necessary ventilatory support while maintaining a shear stress profile similar to that observed during natural breathing. Thus, BiPAP represents a therapeutic option that combines efficacy in alleviating respiratory distress with a lower risk of inducing mechanical stress-related airway damage.

3.4. Area- and time-averaged statistics

Fig. 7 presents a detailed comparative analysis of the area-weighted averages of wall static pressure and shear stress throughout different regions of the respiratory tract under various BiPAP settings, namely 12/8, 16/6, and 18/8 cmH_2O.

The static pressure graph shown in Fig. 7(a) indicates pronounced peaks corresponding to inhalation phases across all airway regions, with these pressures diminishing during exhalation. Notably, the upper airways exhibit consistently higher pressures than the lower airways, suggesting a focused delivery of the therapeutic pressure in the upper respiratory tract, which is the point of interest in cases involving OSA. The variation in pressure profiles across different BiPAP settings illustrates the relationship between the intensity of the IPAP/EPAP setting and the resultant pressure, with higher settings achieving more pronounced pressure peaks. The shear stress graph shown in Fig. 7(b) provides complementary insights, demonstrating that shear stress peaks also coincide with the peak phases of inhalation and exhalation, aligning with times of highest air velocity. Interestingly, despite the varying pressure settings, the shear stress across the upper and lower airways does not differ significantly.

Fig. 8 offers a visualization of time-averaged area-weighted averages of wall static pressure across the respiratory system during the inspiration and expiration phases under IPAP/EPAP of 12/8 cmH_2O setting. The images clearly depict the distribution and magnitude of pressures that the respiratory system endures throughout the breathing cycle,

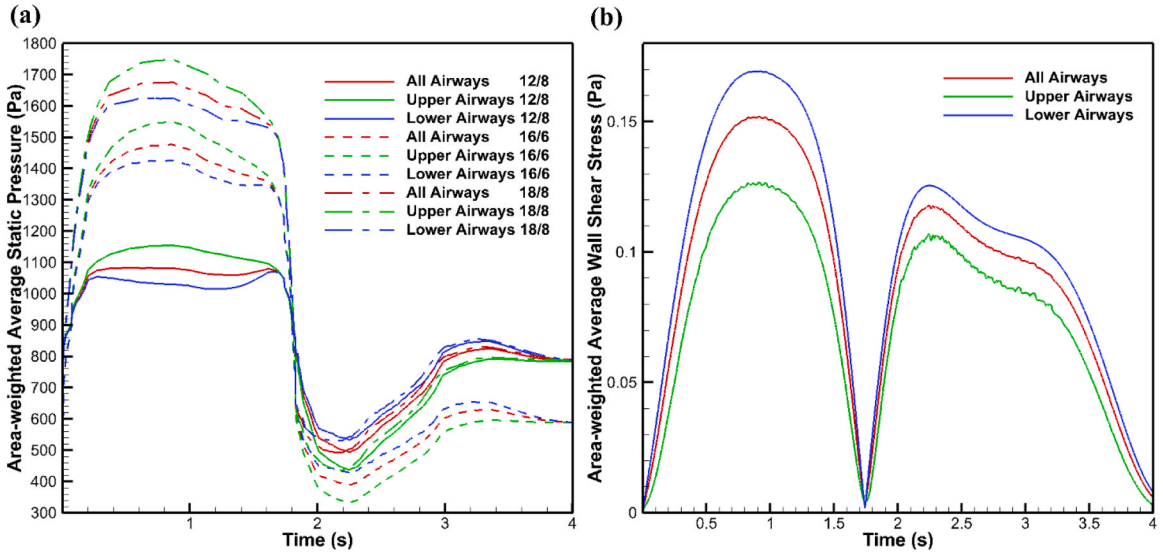

Fig. 7. Area-weighted averages of (a) wall static pressure and (b) shear stress that averages over the upper airways, lower airways, and the entire airways under BiPAP settings.

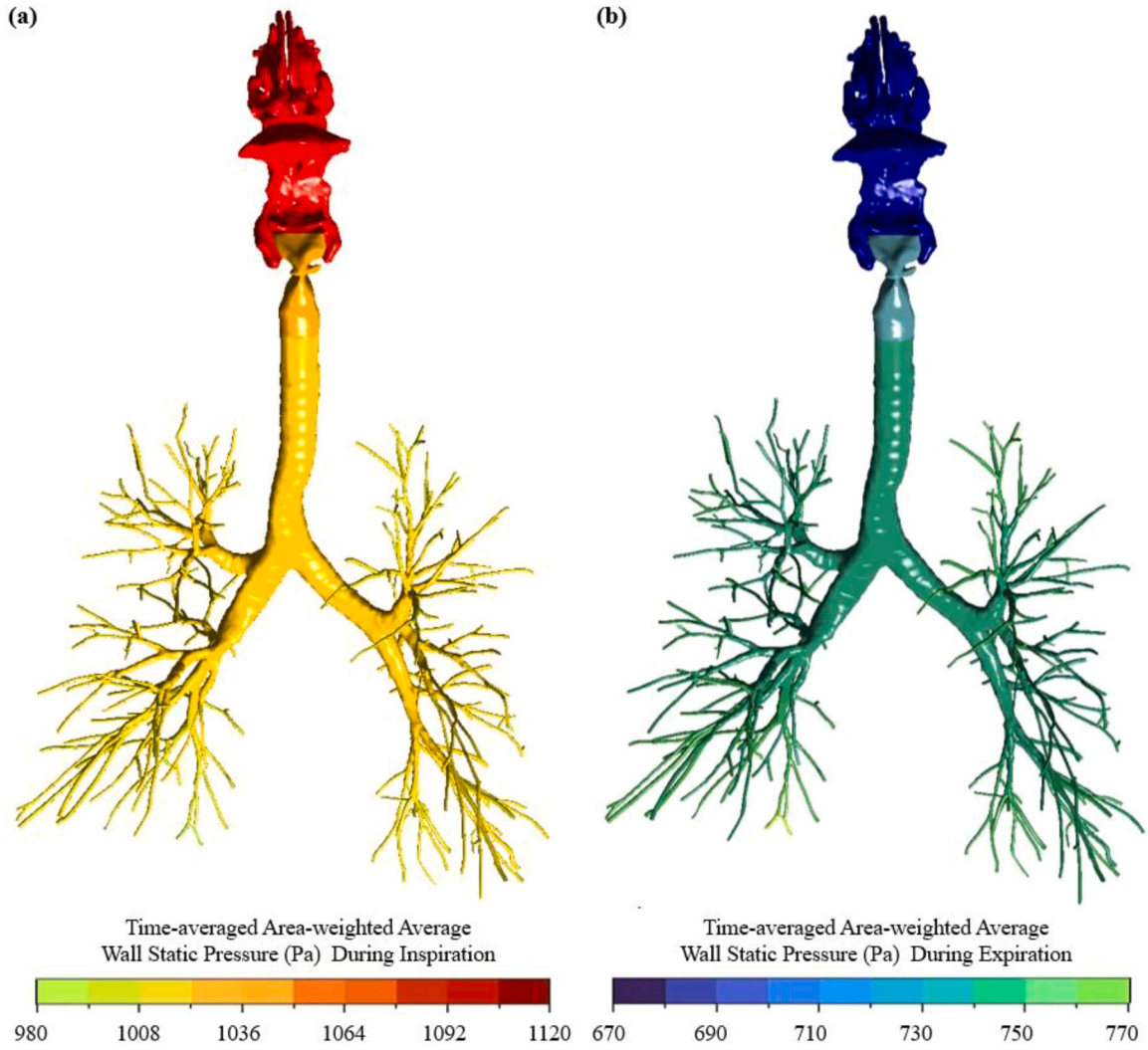

Fig. 8. Visualization of time-averaged area-weighted averages of wall static pressure during (a) inspiration and (b) expiration that averages over the inspiration and expiration period.

Table 1
Time-averaged area-weighted averages of wall static pressure (Pa) that averages over inspiration and expiration period.

	Inspiration				Expiration			
IPAP/EPAP (cmH_2O)	12/8	16/6	18/8	0/0	12/8	16/6	18/8	0/0
Nasal Cavity	1112.78	1423.23	1618.74	−7.44	669.26	514.36	674.46	5.82
Nasopharynx	1111.39	1421.84	1617.35	−8.73	669.56	514.65	674.76	5.98
Oral Cavity	1108.23	1418.68	1614.19	−11.99	670.03	515.14	675.23	6.83
Oropharynx	1107.67	1418.12	1613.63	−12.51	669.47	514.57	674.66	6.37
Laryngopharynx	1105.38	1415.82	1611.33	−14.88	671.46	516.56	676.66	9.05
Larynx	1054.25	1364.69	1560.20	−65.59	700.25	545.41	705.47	39.19
Generation 0	1036.02	1346.47	1541.98	−83.76	722.34	567.49	727.55	61.20
Generation 1	1035.84	1346.29	1541.80	−83.65	723.43	568.58	728.64	62.29
Generation 2	1035.29	1345.73	1541.24	−84.30	723.77	568.92	728.98	62.63
Generation 3	1034.29	1344.73	1540.24	−85.25	724.35	569.50	729.56	63.21
Generation 4	1032.80	1343.24	1538.76	−86.70	725.27	570.42	730.48	64.13
Generation 5	1031.45	1341.89	1537.40	−88.11	725.80	570.95	731.01	64.66
Generation 6	1026.27	1336.72	1532.23	−93.25	729.41	574.56	734.62	68.28
Generation 7	1022.78	1333.23	1528.74	−96.76	733.26	578.40	738.47	72.12
Generation 8	1018.49	1328.93	1524.44	−101.06	736.44	581.59	741.65	75.31
Generation 9	1016.45	1326.89	1522.41	−103.10	737.86	583.01	743.07	76.74
Generation 10	1017.13	1327.57	1523.08	−102.34	739.17	584.32	744.38	78.04
Generation 11	1015.46	1325.90	1521.41	−104.25	740.93	586.08	746.14	79.80
Generation 12	1008.10	1318.55	1514.06	−111.58	745.72	590.87	750.93	84.59
Generation 13	988.80	1299.25	1494.76	−130.99	763.60	608.74	768.81	102.48

providing a critical visual aid in understanding the dynamics of pulmonary mechanics.

In the inspiration phase, the visualization shown in Fig. 8(a) reveals significantly higher pressures within the upper airways, particularly notable in the regions from the nasal cavity to the trachea, illustrated in red and orange hues. These regions, being the primary pathways for air intake, encounter the highest pressures as they work to overcome the resistance of incoming air. As air flows into the branching bronchi, represented in yellow, the pressures moderately decrease. This pressure change, decreasing progressively as the airways bifurcate and extend deeper into the lungs, follows the expected increase in the total cross-sectional area which, in turn, reduces both the airflow velocity and pressure. Conversely, the expiration phase shown in Fig. 8(b) is characterized by notably lower pressures, shown in blue and green colors, reflecting the generally passive nature of this phase where the lung drives the expulsion of air. However, pressures remain comparatively higher near the pharynx, serving a critical role in preventing airway collapse during the reduced pressure conditions that arise during expiration.

Tables 1 and 2 provides a detailed comparison of time-averaged area-weighted averages of wall static pressure and normal force across various sections of the respiratory tract during both the inspiration and expiration phases. This data is presented for different BiPAP settings and contrasted against a scenario without BiPAP (0/0 cmH_2O), thereby illustrating the effectiveness and variations in pressure support provided by BiPAP therapy.

Under the BiPAP settings, there is a notable increase in static pressures and airway wall supporting force during inspiration across all airway locations compared to the without-BiPAP scenario. The higher pressure and forces observed, particularly in the upper airway regions, diminish as air moves toward the lower bronchial generations, reflecting the spread and dilution of air pressure as it travels through the increasingly branched airways.

From the data, it is evident that the setting of IPAP/EPAP at 12/8 cmH_2O can be utilized for its capability to aid in oxygenation by maintaining sufficient distending pressure. This pressure helps to keep the airways open, which is particularly beneficial for patients who require assistance in sustaining open airways during periods of sleep or other states of low respiratory demand, thus preventing airway collapse and ensuring a consistent supply of oxygen. For patients requiring enhanced CO_2 removal, the IPAP/EPAP setting of 16/6 cmH_2O is more appropriate. This setting employs a higher inspiratory pressure to increase tidal volume, thereby enhancing gas exchange, while the lower expiratory pressure reduces the work of breathing by making exhalation easier and more effective. The 18/8 cmH_2O setting combines the attributes of both oxygenation and CO_2 clearance. It is suited for patients with severe respiratory distress who need substantial ventilatory support. This setting offers robust inspiratory pressures to improve oxygen intake and maintain airway patency while also providing a manageable expiratory pressure that aids in efficient CO_2 elimination.

Clinically, the effectiveness of these settings requires careful consideration and tailoring to match the specific respiratory needs of each patient. This involves a dynamic assessment and adjustment based on the patient's tolerance to the therapy and their response to the set pressures. By optimizing the BiPAP settings according to individual patient conditions, clinicians can significantly improve patient comfort, enhance gas exchange, and prevent respiratory complications such as hypoventilation or airway collapse, thereby improving overall treatment outcome.

3.5. BiPAP vs. CPAP

Unlike BiPAP, which provides two discrete levels of pressure during inhalation (IPAP) and exhalation (EPAP), Continuous Positive Airway Pressure (CPAP) delivers a constant, uniform pressure throughout the breathing cycle, primarily targeting airway patency in conditions such as OSA. In our previous study, we simulated a CPAP scenario with a constant positive pressure of 9 cmH_2O (Saha et al., 2024b). Comparing these findings with the 12/8 cmH_2O BiPAP setting reveals that, despite similar flow velocity and wall shear stress stemming from an equivalent volumetric flow rate, the static pressure on the airway wall differs significantly, as shown in Fig. 9. In the CPAP case, this pressure is largely influenced by the interaction between the imposed external pressure and dynamic shifts in alveolar pressure. During inhalation, alveolar pressure is sub-atmospheric, thereby moderating the overall airway wall pressure relative to the constant CPAP level, whereas exhalation raises alveolar pressure above atmospheric levels, resulting in an additive effect with the continuous external pressure. By contrast, BiPAP allows the inspiratory and expiratory pressures to be individually regulated. At 12/8

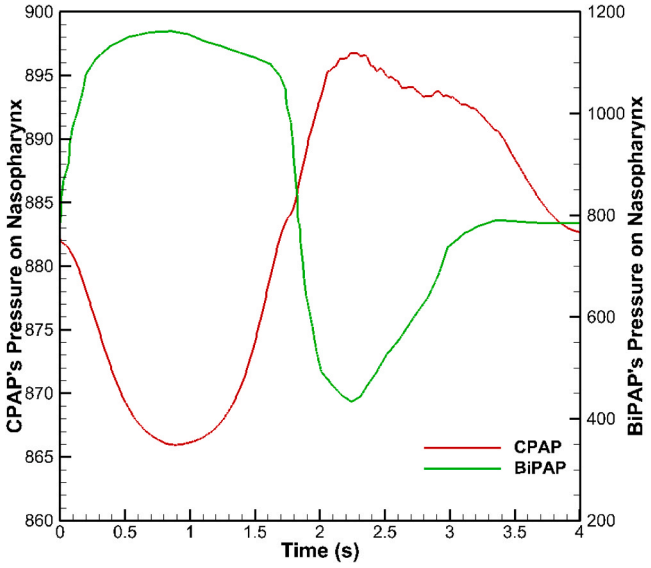

Fig. 9. Time-averaged area-weighted wall static pressure on the nasopharynx wall for two scenarios: CPAP at 9 cmH_2O (red line) and BiPAP at IPAP/EPAP of 12/8 cmH_2O (green line).

Table 2
Time-averaged area-weighted averages of wall normal force (N) that averages over inspiration and expiration period.

	Inspiration				Expiration			
IPAP/EPAP (cmH_2O)	12/8	16/6	18/8	0/0	12/8	16/6	18/8	0/0
Nasal Cavity	17.62	22.53	25.63	−0.12	10.60	8.14	10.68	0.09
Nasopharynx	1.72	2.20	2.50	−0.01	1.04	0.80	1.04	0.01
Oral Cavity	3.74	4.79	5.45	−0.04	2.26	1.74	2.28	0.02
Oropharynx & Laryngopharynx	4.85	6.21	7.07	−0.06	2.94	2.26	2.96	0.03
Larynx	2.21	2.86	3.27	−0.14	1.47	1.14	1.48	0.08
Trachea	5.75	7.47	8.55	−0.46	4.01	3.15	4.04	0.34
Primary Bronchi	2.06	2.68	3.07	−0.17	1.44	1.13	1.45	0.12
Secondary Bronchi	1.76	2.29	2.62	−0.14	1.23	0.97	1.24	0.11
Tertiary Bronchi	2.05	2.67	3.05	−0.17	1.44	1.13	1.45	0.13

cmH_2O, a higher IPAP bolsters alveolar expansion and airway patency during inhalation, followed by a relatively lower EPAP that still maintains sufficient expiratory support. Consequently, the airway wall experiences a pronounced upward pressure trend during inspiration and a corresponding reduction during expiration—opposite to the smoother transition seen in CPAP. Overall, while the absolute magnitudes of CPAP and BiPAP airway pressures can be similar, their distinct pressure profiles highlight the importance of tailored ventilatory strategies to accommodate different respiratory demands and pathophysiological conditions.

4. Conclusions

In conclusion, this study demonstrates that carefully modulating BiPAP settings allows for a more patient-specific approach to noninvasive respiratory support. The tailored IPAP/EPAP combinations not only enhance airway stability and patency, which is particularly vital for preventing collapses in conditions like CSA and OSA but also improve CO_2 clearance and ease of exhalation for COPD patients. Additionally, higher-level support settings can offer simultaneous benefits in oxygenation and CO_2 elimination for OHS cases. Importantly, these adjustments do not introduce excessive mechanical stress on the airway walls, suggesting that BiPAP therapy can be optimized to maintain a favorable biomechanical environment. Collectively, these insights highlight the potential of BiPAP to deliver both physiological efficacy and patient comfort across a range of respiratory disorders, guiding future clinical practices toward more individualized and effective treatment strategies.

Future research

Future research should focus on the extended biomechanical impacts of BiPAP therapy on the respiratory tract to better understand potential tissue adaptation or adverse effects. Such studies are crucial for optimizing therapy, particularly for automatic positive airway pressure therapy that adjusts in response to the dynamic changes in a patient's respiratory needs throughout various sleep stages. Investigating these changes will help in refining these adaptive systems to ensure they not only meet the fluctuating demands effectively but also minimize any negative biomechanical stress that could affect long-term respiratory health.

CRediT authorship contribution statement

Adele Tahan: Writing – review & editing. **Xinlei Huang:** Writing – original draft, Visualization, Validation, Methodology, Investigation, Formal analysis. **Akshoy Ranjan Paul:** Writing – review & editing. **Goutam Saha:** Writing – review & editing, Supervision. **Suvash C. Saha:** Writing – review & editing, Supervision, Project administration, Conceptualization.

Declaration of Competing Interest

The authors have no competing interests to declare that are relevant to the content of this article.

Acknowledgments

The authors acknowledge the computational facilities provided by the University of Technology Sydney (UTS). Additionally, AI-assisted technology (ChatGPT 4) was utilized for language editing and grammar checking. The work of author Xinlei Huang is supported by the China Scholarship Council under Grant ID 202208410137.

Data availability

No data was used for the research described in the article.

References

Agossou, M., Barzu, R., Awanou, B., Bellegarde-Joachim, J., Arnal, J.-M., Dramé, M., 2023. Factors associated with the efficiency of home non-invasive ventilation in patients with obesity-hypoventilation syndrome in Martinique. J. Clin. Med. 12 (10), 3381.

Agrawal, R., Moghtader, S., Ayyala, U., Bandi, V., Sharafkhaneh, A., 2019. Update on management of stable chronic obstructive pulmonary disease. J. Thorac. Dis. 11 (14), S1800.

Al-Abri, M.A., BaHammam, A.S., 2023. Noninvasive ventilation in obesity hypoventilation syndrome: what practitioners need to know? Sleep Vigil. 7 (2), 219–230.

American Academy of Sleep Medicine, Positive Airway Pressure Titration Task Force, et al., 2008. Clinical guidelines for the manual titration of positive airway pressure in patients with obstructive sleep apnea. J. Clin. Sleep Med. 4 (2), 157–171.

ANSYS, 2020b. Transport equations for the standard k-ω model. In: ANSYS Fluent Theory Guide, 4, p. 59.

ANSYS, 2020a. ANSYS Fluent Theory Guide.

Bhatt, S.P., Peterson, M.W., Wilson, J.S., Durairaj, L., 2013. Noninvasive positive pressure ventilation in subjects with stable COPD: a randomized trial. Int. J. Chronic Obstr. Pulm. Dis. 581–589.

Blau, A., Minx, M., Peter, J.G., Glos, M., Penzel, T., Baumann, G., Fietze, I., 2012. Auto bi-level pressure relief–PAP is as effective as CPAP in OSA patients—a pilot study. Sleep Breath. 16, 773–779.

Borel, J.-C., Tamisier, R., Gonzalez-Bermejo, J., Baguet, J.-P., Monneret, D., Arnol, N., Roux-Lombard, P., Wuyam, B., Levy, P., Pépin, J.-L., 2012. Noninvasive ventilation in mild obesity hypoventilation syndrome: a randomized controlled trial. Chest 141 (3), 692–702.

Carotenuto, C., Orlandi, F., Montorsi, L., Milani, M., 2023. CFD With Fluid Structure Interaction Analysis of Lung Alveolar Sacs and its Applications in Emphysema Study, translated by American Society of Mechanical Engineers, V005T06A001.

Chen, S., Wang, J., Liu, D., Lei, L., Wu, W., Liu, Z., Lee, C., 2021. Open oral cavity has little effects on upper airway aerodynamics in children with obstructive sleep apnea syndrome: a computational fluid dynamics study based on patient-specific models. J. Biomech. 121, 110383.

Donovan, L.M., Kapur, V.K., 2016. Prevalence and characteristics of central compared to obstructive sleep apnea: analyses from the sleep heart health study cohort. Sleep 39 (7), 1353–1359.

Dunlap, J.T., Glassford, M., Hopkins, L.W., 2023. Chronic obstructive pulmonary disease, obstructive sleep apnea, and heart failure. In: Hayes, K.M.S., Dellise, N.R. (Eds.), Managing Heart Failure in Primary Care: A Case Study Approach. Springer International Publishing, Cham, pp. 205–223.

Funk, G.-C., Breyer, M.-K., Burghuber, O.C., Kink, E., Kirchheiner, K., Kohansal, R., Schmidt, I., Hartl, S., 2011. Long-term non-invasive ventilation in COPD after acute-on-chronic respiratory failure. Respir. Med. 105 (3), 427–434.

Gay, P.C., Herold, D.L., Olson, E.J., 2003. A randomized, double-blind clinical trial comparing continuous positive airway pressure with a novel bilevel pressure system for treatment of obstructive sleep apnea syndrome. Sleep 26 (7), 864–869.

GeomagicWrap, 2022. Geomagic Wrap Overview.

Gökcan, M.K., Kurtuluş, D.F., Aypak, A., Köksal, M., Ökten, S.R., 2024. Insights from 3D modeling and fluid dynamics in COVID-19 pneumonia. Med. Biol. Eng. Comput. 62 (2), 621–636.

Gunatilaka, C.C., Schuh, A., Higano, N.S., Woods, J.C., Bates, A.J., 2020. The effect of airway motion and breathing phase during imaging on CFD simulations of respiratory airflow. Comput. Biol. Med. 127, 104099.

Hu, P., Cai, C., Yi, H., Zhao, J., Feng, Y., Wang, Q., 2022. Aiding airway obstruction diagnosis with computational fluid dynamics and convolutional neural network: a new perspective and numerical case study. J. Fluids Eng. 144 (8), 081206.

Huang, X., Clemon, L.M., Islam, M.S., Saha, S.C., 2022. Optimization of fluid characteristics in the main nozzle of an air-jet loom. Text. Res. J. 92 (3–4), 525–538.

Huang, X., Francis, I., Saha, G., Rahman, M.M., Saha, S.C., 2024a. Large eddy simulation-based modeling of cold-air inhalation from nasal cavities to the distal lung: insights for athlete health and performance. Results Eng., 102475

Huang, X., Saha, S.C., Saha, G., Francis, I., Luo, Z., 2024b. Transport and deposition of microplastics and nanoplastics in the human respiratory tract. Environ. Adv. 16, 100525.

Iwasaki, T., Sugiyama, T., Yanagisawa-Minami, A., Oku, Y., Yokura, A., Yamasaki, Y., 2020. Effect of adenoids and tonsil tissue on pediatric obstructive sleep apnea severity determined by computational fluid dynamics. J. Clin. Sleep Med. 16 (12), 2021–2028.

Javaheri, S., Badr, M.S., 2022. Central sleep apnea: pathophysiologic classification. Sleep 46 (3).

Kadota, K., Matsumoto, K., Uchiyama, H., Tobita, S., Maeda, M., Maki, D., Kinehara, Y., Tachibana, I., Sosnowski, T.R., Tozuka, Y., 2022. In silico evaluation of particle transport and deposition in the airways of individual patients with chronic obstructive pulmonary disease. Eur. J. Pharm. Biopharm. 174, 10–19.

Masa, J.F., Corral, J., Alonso, M.L., Ordax, E., Troncoso, M.F., Gonzalez, M., Lopez-Martínez, S., Marin, J.M., Marti, S., Díaz-Cambriles, T., 2015. Efficacy of different treatment alternatives for obesity hypoventilation syndrome. Pickwick study. Am. J. Respir. Crit. Care Med. 192 (1), 86–95.

Masa, J.F., Corral, J., Caballero, C., Barrot, E., Terán-Santos, J., Alonso-Álvarez, M.L., Gomez-Garcia, T., González, M., López-Martín, S., De Lucas, P., 2016. Non-invasive ventilation in obesity hypoventilation syndrome without severe obstructive sleep apnoea. Thorax 71 (10), 899–906.

McNicholas, W.T., 2009. Chronic obstructive pulmonary disease and obstructive sleep apnea: overlaps in pathophysiology, systemic inflammation, and cardiovascular disease. Am. J. Respir. Crit. Care Med. 180 (8), 692–700.

Medical, M.M., 2021. Mimics Medical 24.0 – Instructions for Software Use.

Nishi, M., 2004. Breathing of Humans and its Simulation, LSTM-Erlangen Institute of Fluid Mechanic Friedlich-Alexander-University Erlangen.

Nomura, T., Horikoshi, T., Kitano, Y., Yamada, M., Kondo, K., Kikuchi, S., 2022. Postoperative functional evaluation of obstructive sleep apnea syndrome by computational fluid dynamics. Indian J. Otolaryngol. Head Neck Surg. 74 (3), 5044–5051.

Olson, A.L., Zwillich, C., 2005. The obesity hypoventilation syndrome. Am. J. Med. 118 (9), 948–956.

Paone, G., Conti, V., Biondi-Zoccai, G., De Falco, E., Chimenti, I., Peruzzi, M., Mollica, C., Monaco, G., Giannunzio, G., Brunetti, G., 2014. Long-term home noninvasive mechanical ventilation increases systemic inflammatory response in chronic obstructive pulmonary disease: a prospective observational study. Mediat. Inflamm. 2014 (1), 503145.

Pazarli, A.C., Köseoğlu, H.I., 2023. Devices for CPAP in OSA. Noninvasive Mechanical Ventilation: Theory, Equipment, and Clinical Applications. Springer, pp. 273–281.

Petty, T.L., 2006. The history of COPD. Int. J. Chronic Obstr. Pulm. Dis. 1 (1), 3–14.

Raherison, C., Girodet, P., 2009. Epidemiology of COPD. Eur. Respir. Rev. 18 (114), 213–221.

Ren, S., Li, W., Wang, L., Shi, Y., Cai, M., Hao, L., Luo, Z., Niu, J., Xu, W., Luo, Z., 2020. Numerical analysis of airway mucus clearance effectiveness using assisted coughing techniques. Sci. Rep. 10 (1), 2030.

Ryu, S., Kim, J.H., Yu, H., Jung, H.-D., Chang, S.W., Park, J.J., Hong, S., Cho, H.-J., Choi, Y.J., Choi, J., 2021. Diagnosis of obstructive sleep apnea with prediction of flow characteristics according to airway morphology automatically extracted from medical images: computational fluid dynamics and artificial intelligence approach. Comput. Methods Prog. Biomed. 208, 106243.

Saha, S.C., Francis, I., Huang, X., Paul, A., 2022a. Heat transfer and fluid flow analysis of realistic 16-Generation lung. Phys. Fluids 34 (6).

Saha, S.C., Francis, I., Huang, X., Rahman, M.M., 2022b. Fluid-particle dynamics of nasal drug delivery in a realistic human airway lung model, translated by.

Saha, S.C., Francis, I., Saha, G., Huang, X., Molla, M.M., 2024a. Hemodynamic insights into abdominal aortic aneurysms: bridging the knowledge gap for improved patient care. Fluids 9 (2), 50.

Saha, S.C., Huang, X., Francis, I., Saha, G., 2024b. Airway stability in sleep apnea: assessing continuous positive airway pressure efficiency. Respir. Physiol. Neurobiol. 325, 104265.

Sanchez, A.M., Germany, R., Lozier, M.R., Schweitzer, M.D., Kosseifi, S., Anand, R., 2020. Central sleep apnea and atrial fibrillation: a review on pathophysiological mechanisms and therapeutic implications. IJC Heart Vasc. 30, 100527.

Siemens, 2017. NX 12 Release Notes.

Singh, D., Agusti, A., Anzueto, A., Barnes, P.J., Bourbeau, J., Celli, B.R., Criner, G.J., Frith, P., Halpin, D.M., Han, M., 2019. Global strategy for the diagnosis, management, and prevention of chronic obstructive lung disease: the GOLD science committee report 2019. Eur. Respir. J. 53 (5).

Taherian, S., Rahai, H., Lopez, S., Shin, J., Jafari, B., 2019. Evaluation of human obstructive sleep apnea using computational fluid dynamics. Commun. Biol. 2 (1), 423.

Tung, P., Anter, E., 2016. Atrial fibrillation and sleep apnea: considerations for a dual epidemic. J. Atr. Fibrillation 8 (6).

Tung, P., Levitzky, Y.S., Wang, R., Weng, J., Quan, S.F., Gottlieb, D.J., Rueschman, M., Punjabi, N.M., Mehra, R., Bertisch, S., 2017. Obstructive and central sleep apnea and the risk of incident atrial fibrillation in a community cohort of men and women. J. Am. Heart Assoc. 6 (7), e004500.

Wedel, J., Steinmann, P., Štrakl, M., Hriberšek, M., Cui, Y., Ravnik, J., 2022. Anatomy matters: the role of the subject-specific respiratory tract on aerosol deposition - a CFD study. Comput. Methods Appl. Mech. Eng. 401, 115372.

Yang, X., Xiao, Y., Han, B., Lin, K., Niu, X., Chen, X., 2019. Implication of mixed sleep apnea events in adult patients with obstructive sleep apnea-hypopnea syndrome. Sleep Breath. 23, 559–565.

Young, R., Benjamin, A., 2023. The assessment and management of obstructive sleep apnoea–hypopnoea syndrome and obesity hypoventilation syndrome in obesity. Clin. Med. 23 (4), 372–379.

Zhang, D., Guan, Y., Zhou, X., Zhang, M., Pu, Y., Gu, P., Xia, Y., Lu, Y., Chen, J., Tu, W., 2024. Aerodynamic simulation of small airway resistance: a new imaging biomarker for chronic obstructive pulmonary disease. Int. J. Chronic Obstr. Pulm. Dis. 1167–1175.